nature communications

Article

https://doi.org/10.1038/s41467-026-69324-0

Phosphine-mediated hydrogen bond and phosphorescence energy transfer for tunable chiroptical afterglow in stacked polymers

Received: 12 July 2025

Accepted: 29 January 2026

Published online: 10 February 2026

Check for updates

Zhisheng Gao[1], Shuai Huang[2], Xiaona Lian[1], Xin Yan[1], Hengyu Cao[1], Shuman Zhang[1], Peng Zhang[1], Qi Jia[1], Huanhuan Li[1] ✉, Hui Li[1], Runfeng Chen[1], Gaozhan Xie[1], Yun Ma[1], Ting Wang[1], Wei Huang[1,3] ✉ & Ye Tao[1] ✉

Polymer-doped chiral organic afterglow (COA) materials represent an emerging frontier in photonics, yet their development is constrained by weak hydrogen bond interactions and limited spectral diversity. Herein, a supramolecular engineering strategy utilizing phosphonic acid-derived directional hydrogen bond networks is proposed to construct COA materials. Leveraging the tetrahedral coordination geometry and dual proton-donor functionality of phosphonic acid derivatives, a robust three-dimensional hydrogen bond network is formed with polyvinyl alcohol, yielding blue afterglow emission with a lifetime of 3.05 s, a photoluminescence quantum yield of 33.3%, and enhanced thermal stability. Structural and computational analyses reveal that near-linear hydrogen bond geometry and orbital hybridization synergistically enhance the hydrogen bond strength while enabling chiral amplification by an interfacial chiral polylactic acid coating. Furthermore, through efficient phosphorescence energy transfer, multicolor COA emissions are achieved in stacked polymeric films, exhibiting dissymmetry factors up to 0.03 and afterglow emissions across the visible spectra, allowing the development of customizable encryption inks with spatiotemporal resolved chiroptical signatures for multiple applications. This work not only thoroughly investigates the modulation of hydrogen bonds on afterglow properties but also provides a fundamental understanding of non-covalent interactions in organic optoelectronics.

Chiral organic afterglow (COA) materials have garnered significant attention in next-generation optoelectronics due to their unique integration of persistent luminescence with chiroptical activity[1–7], enabling applications in anti-counterfeiting encryption[8–11], chiroptical analysis[12–14], and stereoscopic displays[15,16]. While crystal engineering and supramolecular self-assembly strategies have demonstrated potential in constructing COA systems through π–π stacking optimization and vibrational suppression[17–20], these approaches face inherent limitations in spectral tunability and intricate synthesis procedures. Polymer-based host-guest doping systems emerge as a versatile alternative, where hydrogen bond networks can simultaneously immobilize emitters to suppress non-radiative decay and flexibly modulate chiral and emissive properties through host-guest interactions[21–24]. However, conventional COA materials

[1]State Key Laboratory of Flexible Electronics (LoFE) & Institute of Advanced Materials (IAM), Nanjing University of Posts & Telecommunications, Nanjing, China. [2]Dongying Hebang Chemical Co., Ltd, Dongying, Shandong, China. [3]Frontiers Science Center for Flexible Electronics (FSCFE), MIIT Key Laboratory of Flexible Electronics (KLoFE), Northwestern Polytechnical University, Xi'an, Shaanxi, China. ✉e-mail: iamhhli@njupt.edu.cn; vc@nwpu.edu.cn; iamytao@njupt.edu.cn

predominantly rely on hydrogen bonds mediated by carboxyl[25,26], boronic acid[27–30], and/or hydroxyl groups[31–33]. These interactions, though effective, often suffer from limited strength, particularly under elevated temperatures, restricting their ability to support high-efficiency and long-lifetime afterglow[34,35]. Therefore, there is an urgent need to explore alternative hydrogen bond motifs that offer stronger intermolecular interactions to enhance COA performance.

Principally, critical to this paradigm is the precise engineering of hydrogen bond strength and geometry, which is directly governed by the electronegativity of hydrogen bond acceptor that can be modulated by the connected atoms (X) and linear spatial arrangement of hydrogen bond (Fig. 1a)[36–38]. Phosphoric acid derivatives bearing the tetrahedral coordination geometry and dual proton-donor functionality are promising candidates for developing hydrogen bond networks. Previous report has revealed that phosphate-mediated hydrogen bonds achieve near-linear alignment ($\theta \approx 175°$), combining three-dimensional networking capacity and binding energies exceeding 25 kJ mol^{-1} due to the orbital coupling and delocalization[39–42], which may enable enhanced hydrogen bond strength for constructing COA materials with improved efficiency and lifetime. Guided by these principles, (2-(9H-carbazol-9-yl)ethyl)phosphonic acid (2PACz) containing phosphate groups is selected as the luminescent anchoring molecule. The phosphate groups endow a directional and multi-dimensional hydrogen bond network with hydroxyls of polyvinyl alcohol (PVA), enabling the suppression of molecular vibration induced exciton quenching (Fig. 1b). The prepared film achieves a blue organic afterglow with a main emission peak at 444 nm, lifetime of 3.05 s, and photoluminescence quantum yield (PLQY) of 33.3%. More importantly, compared to the carboxylic acid engineered hydrogen bond counterpart, 2PACz-doped PVA films exhibit much enhanced thermal stability. Meanwhile, by spinning chiral polylactic acid (PLA) on 2PACz-doped PVA (2PACz@PVA) films, a universal method for constructing COA emission is achieved, showing a maximum dissymmetry factor (g_{lum}) of 0.03. By utilizing a Förster resonance energy transfer (FRET) process, green, yellow, and red chiral afterglow emissions are achieved (Fig. 1c) through doping various fluorescence emitters into 2PACz@PVA@PLA films, thus empowering versatile afterglow inks for coating and encryption applications. These results

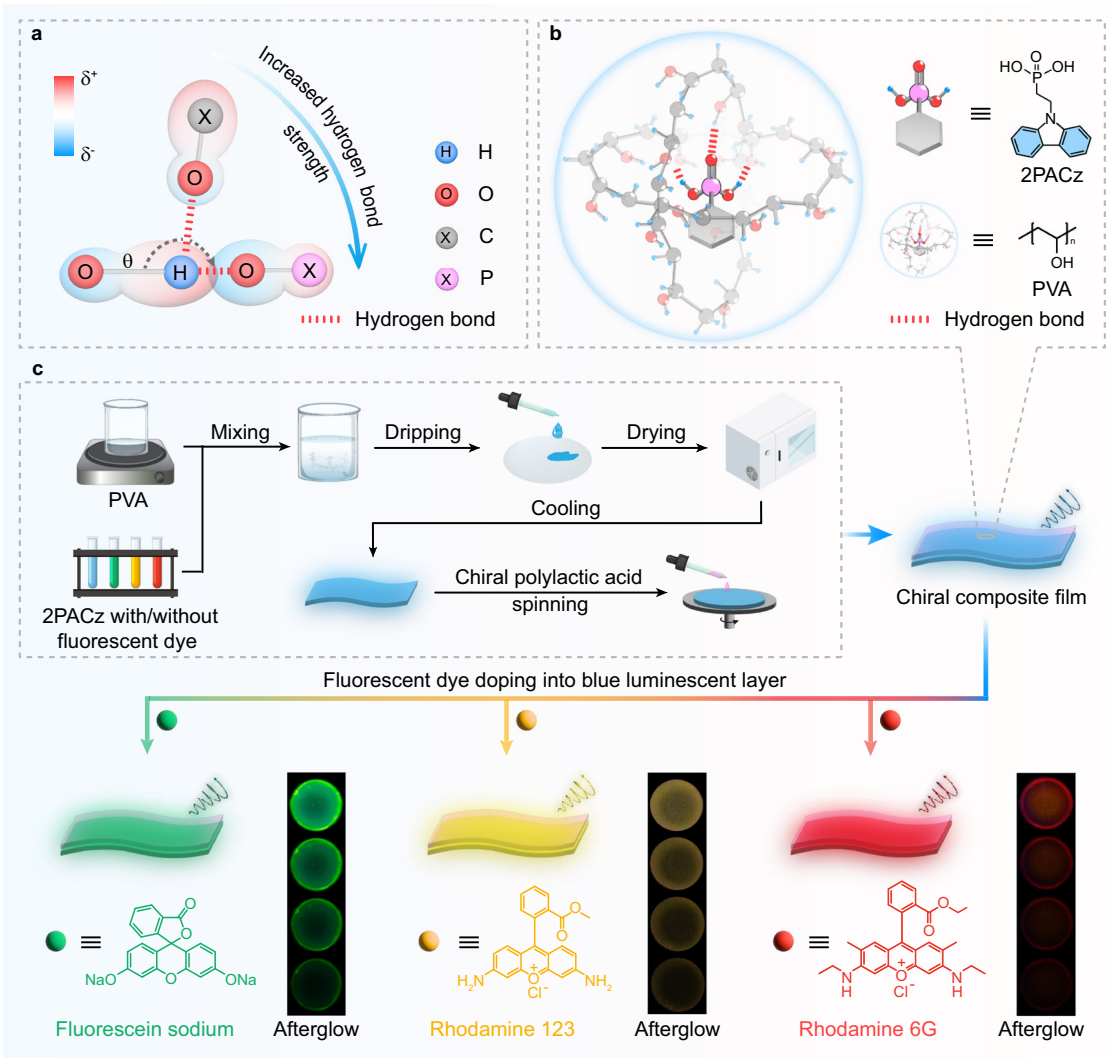

Fig. 1 | Schematic diagram for constructing multicolor chiral organic afterglow (COA) by hydrogen bond mediation and phosphorescence energy transfer. **a** Principle drawing for hydrogen bond strength mediation through modulating electronegativity of hydrogen bond acceptor and spatial arrangement of hydrogen bond. **b** Formation of a three-dimensional hydrogen bond network mediated by phosphorus in polyvinyl alcohol (PVA) film and the molecular structure of 2PACz and PVA. **c** Preparation procedure and corresponding afterglow photographs of multi-color COA films, as well as the molecular structures of the incorporated multi-color fluorescence emitters.

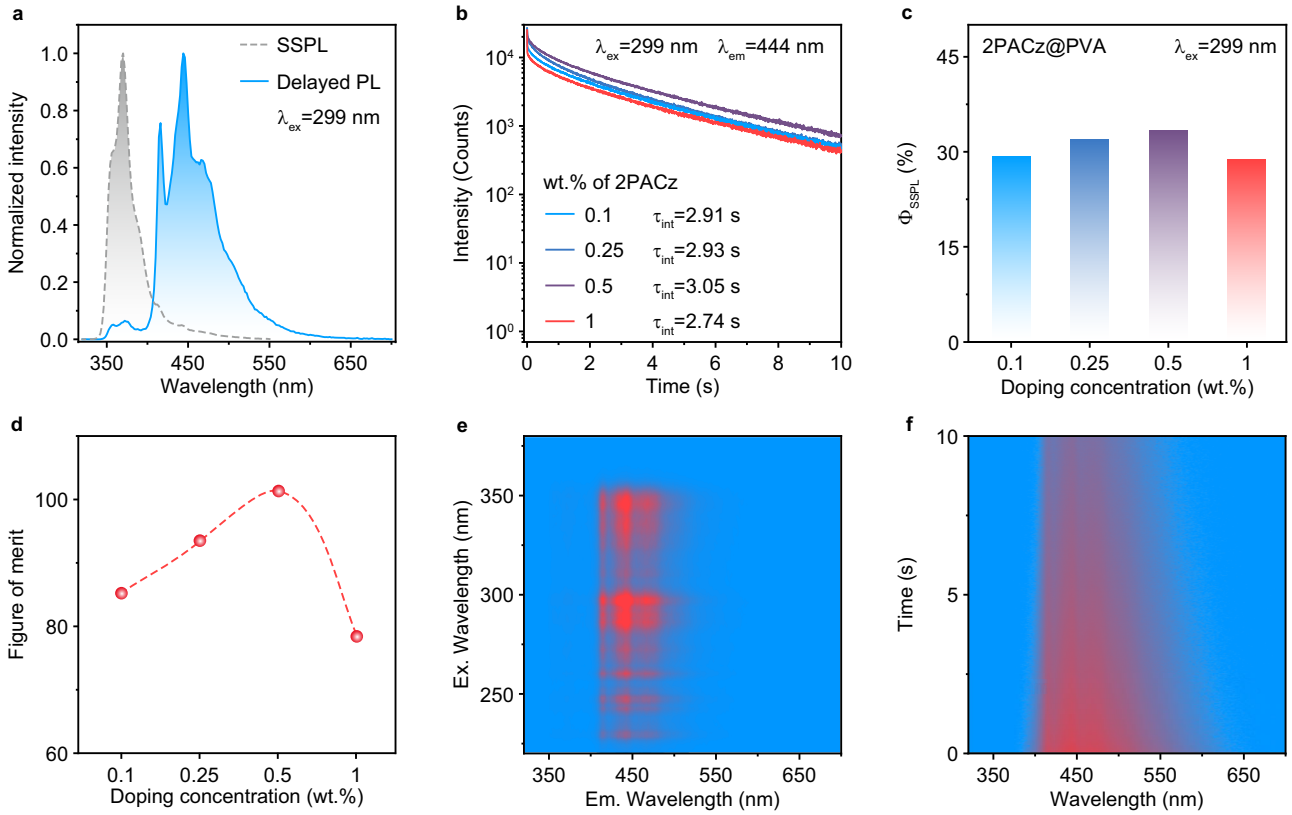

Fig. 2 | Photophysical property of 2PACz@PVA. a Steady-state photoluminescence (SSPL) and delayed PL spectra of 0.5 wt.% 2PACz@PVA film. Lifetimes (**b**), photoluminescence quantum yields (**c**), and figure of merit (**d**) of 2PACz@PVA films at different doping concentrations. **e** Excitation-delayed PL emission mapping of 0.5 wt.% 2PACz@PVA film with a delayed time of 25 ms. **f** Time-resolved emission spectrum of 0.5 wt.% 2PACz@PVA film.

not only provide a deep understanding to modulate the hydrogen bond interactions but also propose a feasible method to develop advanced COA materials for various applications.

Results

Synthesis and characterization

Phosphonic acid modified carbazole derivatives, 2PACz and (4-(9H-carbazol-9-yl)butyl)phosphonic acid (4PACz), were synthesized in three steps with high yields, and their molecular structures were determined by ^{1}H, ^{13}C, ^{31}P-nuclear magnetic resonance (NMR) and high-resolution mass spectrometry (Supplementary Fig. 1 and Supplementary Figs. 3–22). Additionally, a control molecule, a carboxylic acid modified carbazole derivative, (2-(9H-carbazol-9-yl)ethyl) carboxylic acid (2CACz), was synthesized to demonstrate the better of phosphonic acid groups in constructing strong hydrogen bond networks (Supplementary Fig. 2 and Supplementary Figs. 23–28). The melting temperatures of 2PACz, 4PACz, and 2CACz are 240, 285, and 175°C, respectively (Supplementary Fig. 29). Generally, 2PACz@PVA film was prepared by evaporating the mixture of 2PACz ethanol solution and PVA aqueous solution. Through regulating the concentrations of 2PACz ethanol solution, 2PACz@PVA films with different doping concentrations could be easily achieved. 4PACz@PVA and 2CACz@PVA films with different doping concentrations were prepared by the same method (Supplementary Fig. 30). Thermogravimetric analysis of the 2PACz@PVA, 4PACz@PVA and 2CACz@PVA films shows no significant mass loss up to 200°C (Supplementary Fig. 31), and no ethanol peaks are detected in the ^{1}H NMR spectrum of the 2PACz@PVA film (Supplementary Fig. 32). These results collectively exclude any influence of volatile solvents on the observed luminescence properties.

Photophysical properties investigation

2PACz shows characteristic absorption and fluorescence features of carbazole in tetrahydrofuran solution, with a maximum absorption peak at 290 nm and emission peaks at 350 and 370 nm (Supplementary Fig. 33). The steady-state photoluminescence (SSPL) and delayed PL spectra of 2PACz@PVA films with different doping concentrations (0.1–1.0 wt.%) exhibit main fluorescence and afterglow emission peaks at 370 and 444 nm, respectively (Fig. 2a and Supplementary Figs. 34 and 35). Intense blue afterglow emission can be captured by a commercial camera for 30 s (Supplementary Fig. 36). Among these films, 0.5 wt.% 2PACz@PVA film achieves the highest fluorescence intensity, PLQY of 33.3% as well as the most pronounced afterglow intensity and longest afterglow lifetime (τ_A, 3.05 s) (Fig. 2b, c and Supplementary Table 1). Consequently, 0.5 wt.% 2PACz@PVA film demonstrates the best figure of merit, defined as Q_{FM} = PLQY×τ_A (Fig. 2d and Supplementary Table 1). Excitation-delayed PL emission mapping spectra (Fig. 2e) highlight a fixed afterglow emission peak at 444 nm upon excitation with 220-350 nm UV light, which is further corroborated by the time-resolved emission spectra (TRES) (Fig. 2f). The low-temperature delayed PL spectra of 2PACz in methyl tetrahydrofuran solution (Supplementary Fig. 37) exhibit identical emission behavior to that of the 0.5 wt.% 2PACz@PVA film, underscoring the isolated emission nature of the doped film.

Afterglow mechanism analysis

To further investigate the afterglow properties of 2PACz@PVA, a series of control experiments was conducted, focusing on variations in the alkane chain length (4PACz) and the end groups (2CACz) of 2PACz. As shown in Fig. 3a and Supplementary Fig. 38a, the delayed PL emission peaks of 0.5 wt.% 4PACz and 0.5 wt.% 2CACz-doped PVA films are

https://doi.org/10.1038/s41467-026-69324-0

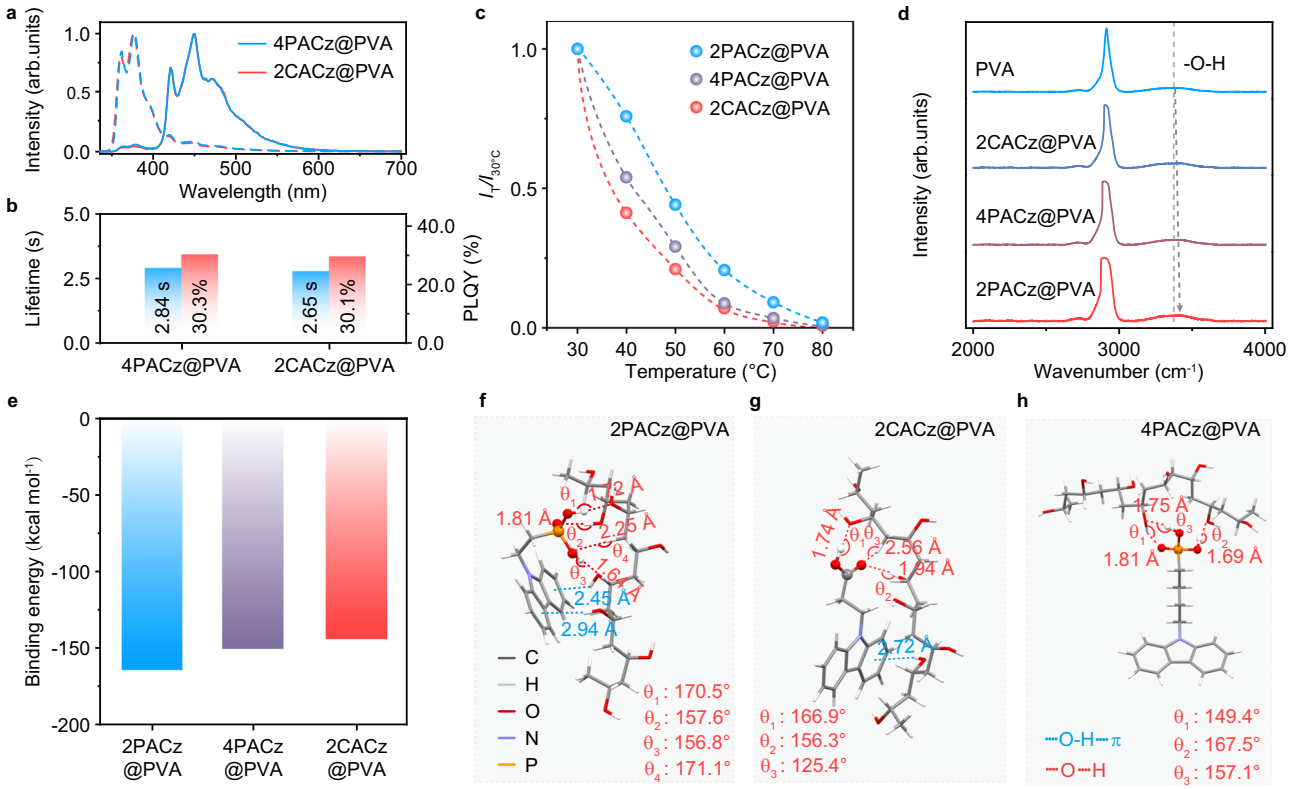

Fig. 3 | Intermolecular interaction investigations. a SSPL (dashed line) and delayed PL (solid line) spectra of 4PACz@PVA and 2CACz@PVA films with 0.5 wt.% doping concentrations; **b** Lifetime, photoluminescence quantum yield (PLQY) of 0.5 wt.% 4PACz@PVA and 0.5 wt.% 2CACz@PVA films. **c** Temperature-dependent delayed PL intensity ratios ($I_T/I_{30°C}$) of 0.5 wt.% 2PACz@PVA, 0.5 wt.% 4PACz@PVA and 0.5 wt.% 2CACz@PVA films. **d** Raman spectra of PVA, 0.5 wt.% 2PACz@PVA, 0.5 wt.% 4PACz@PVA and 0.5 wt.% 2CACz@PVA films. Calculated intermolecular binding energies (**e**) and interactions (**f**–**h**) of 2PACz@PVA (**e**, **f**), 2CACz@PVA (**e**, **g**), and 4PACz@PVA (**e**, **h**).

almost identical to that of 2PACz@PVA film. These results suggest that the modulation of alkane chain length and end groups has a limited impact on the triplet properties of the carbazole chromophore. Notably, 2PACz@PVA film exhibits enhanced afterglow intensities and lifetimes compared to those of 4PACz and 2CACz-doped PVA films. Specifically, the 0.5 wt.% 4PACz and 2CACz doped PVA films show lifetimes of 2.84 s and 2.65 s as well as PLQYs of 30.3% and 30.1% (Fig. 3b and Supplementary Fig. 38b). This enhanced performance can be attributed to the additional n-π* transition contribution by the oxygen atom in P=O in the frontier molecular orbital distributions of 2PACz (Supplementary Fig. 39), thus enabling a much larger spin-orbit coupling constant of T_1-S_0 of 2PACz than that of 4PACz and 2CACz (Supplementary Fig. 40). Therefore, the 2PACz@PVA film demonstrates a higher Q_{FM}, underscoring its more exceptional and efficient luminescent properties (Supplementary Fig. 41). The temperature-dependent PL intensity variations illustrate the thermal stabilities of PL spectra for 0.5 wt.% 2PACz@PVA, 4PACz@PVA and 2CACz@PVA films, indicating the comparative quenching behavior of afterglow emission at elevated temperatures (Fig. 3c and Supplementary Fig. 42). Notably, with increasing temperatures, the 2PACz@PVA film retains slightly much higher intensities than the others, highlighting its much improved thermal stability. Furthermore, the doped films exhibit stable afterglow at various temperatures (77–343 K) (Supplementary Fig. 43). The afterglow remains constant over time at 25% relative humidity, whereas at 90% humidity, moisture disrupts the hydrogen bond network in the film. This leads to the enhanced molecular vibrations and triplet excitons quenching, which significantly reduces afterglow intensity (Supplementary Fig. 44). The prepared 2PACz@PVA, 4PACz@PVA, and 2CACz@PVA films only display typical powder X-ray diffraction (XRD) patterns at 19°, which is attributed to the crystallization of PVA (Supplementary Fig. 45)[43,44]. This is further supported by wide-angle X-ray scattering (WAXS) measurements, which show scattering peaks solely at 1.37 $Å^{-1}$ originating from PVA (Supplementary Fig. 46)[45]. No additional XRD and WAXS peaks are found, suggesting the isolated chromophore nature in PVA doped films. The energy dispersive X-ray spectroscopy and elemental mapping images of 0.5 wt.% 2PACz@PVA film confirms the homogeneous dispersion of 2PACz within the PVA matrix, as evidenced by the uniform distribution of its characteristic N and P signals (Supplementary Fig. 47). Furthermore, owing to the homogeneous dispersion of chromophore in PVA films, SSPL spectra and afterglow quantum yields of multiple independently prepared 2PACz@PVA, 4PACz@PVA and 2CACz@PVA films demonstrate high reproducibility (Supplementary Fig. 48 and Table 2). Compared to the O-H vibrational peaks at 3310 cm^{-1} of Raman spectra and at 3430 cm^{-1} of Fourier transform infrared (FTIR) in PVA film, slight blue shifted peak are observed in the FTIR (Supplementary Fig. 49 and Supplementary Fig. 50a) and Raman spectra (Fig. 3d and Supplementary Fig. 50b) of 2PACz@PVA, 4PACz@PVA, and 2CACz@PVA films[46–49]. Notably, 2PACz@PVA film demonstrates the most significant blue shift, indicating stronger hydrogen bond interaction between 2PACz and the PVA matrix. Meanwhile, the enhancement of hydrogen bond interaction also leads to the broadening of C-H stretching vibration[47] at 2910 cm^{-1}. This enhanced intermolecular interaction may play a vital role in endowing the improved afterglow properties of the isolated 2PACz molecules within the composite films. This important role of intermolecular interaction is further verified by varied polymeric matrices. Only SSPL could be captured when 2PACz, 4PACz, and 2CACz are doped into a non-polar polystyrene matrix, respectively (Supplementary Fig. 51). In contrast, the stronger and more abundant hydrogen bonds in polar

polymeric matrices directly enhance both the SSPL and delayed PL intensities compared to their non-polar and weakly polar polymeric counterparts (Supplementary Fig. 52).

To gain deeper insight into the variations in intermolecular interactions, theoretical calculations were performed. The hydrogen bond strength in the molecular structure, which significantly impacts its photophysical properties, is influenced by the electronic effects such as electronegativity and molecular geometry[50,51]. The lower electronegativity of the phosphorus atom in the phosphate acid group results in a higher negative charge density on the oxygen atom in P=O and O-H of 2PACz compared to the oxygen atom in C=O and O-H of 2CACz (Supplementary Fig. 53 and Table 3), while the hydrogen atom on the hydroxyl group in 2PACz exhibits a higher positive charge density than that in 2CACz. The higher electrostatic potential (ESP) of the carbazole unit in 2PACz, compared to those in 4PACz and 2CACz, corresponds to its stronger computed binding energy with PVA (−282.65 kcal mol^{-1}) (Supplementary Figs. 53 and 54, and Table 3). Furthermore, the phosphonic acid reveals more positive ESP values in 2PACz compared to the carboxyl group in 2CACz, which confers a higher binding energy between phosphonic acid and PVA (Supplementary Figs. 53 and 55, and Table 3). The directional interactions between 2PACz and PVA promote the formation of more linear hydrogen bonds, showing intersection angles between O-H···O of 156.8°, 157.6°, 170.5°, and 171.1°. These results lead to shorter and stronger hydrogen bond (Fig. 3e, f) as well as higher binding energy (Fig. 3e and Supplementary Fig. 56a–c) in 2PACz compared to those in 2CACz (Fig. 3g). In contrast, the long alkyl chain in 4PACz diminishes the electron-donating ability of the carbazole group. Consequently, the negative charge density of the oxygen atoms in the P=O and O-H groups of 4PACz is reduced (Supplementary Table 3), along with the reduced positive charge density on the hydrogen atom of the hydroxyl group. These results weaken the hydrogen bond interactions between 4PACz and PVA, as further evidenced by longer distances and smaller O-H···O intersection angles of 149.4°, 157.1°, and 167.5° (Fig. 3h) compared to those in the 2PACz@PVA film. Moreover, the extended alkyl chain in 4PACz hinders the formation of O-H···π type hydrogen bond between the PVA hydroxyl groups and the luminescent groups, which is a feature molecular interaction observed in 2PACz and 2CACz, resulting in weaker thermal stability for 4PACz[52,53]. Moreover, upon increasing the number of PVA chains from single to two and three, the binding energies between 2PACz and PVA are consistently higher than those of 4PACz and PVA (Supplementary Fig. 56d–i). Combining experimental and theoretical calculation results, the phosphine-mediated hydrogen bond interaction in 2PACz@PVA film plays a pivotal role in the construction of afterglow materials with improved luminescent features within the composite films.

Multicolor afterglow emission construction

Considering the ultralong lifetime of 3.05 s, blue afterglow emission with a wide range of 350–600 nm, as well as the good solubility and flexibility of 0.5 wt.% 2PACz@PVA film, this doped film could be a promising afterglow energy donor to construct versatile and colorful afterglow systems (Fig. 4a). Experimentally, water-soluble fluorescent dyes including fluorescein sodium (Fluc), rhodamine 123 (Rh123) and rhodamine 6G (Rh6G) were chosen as energy acceptors owing to the significant overlap between their absorption spectra and the delayed PL spectrum of 0.5 wt.% 2PACz@PVA film (Fig. 4b)[26,54,55]. The SSPL and delayed PL exhibit peaks at 538, 565, and 600 nm in Fluc@2-PACz@PVA, Rh123@2PACz@PVA, and Rh6G@2PACz@PVA (Fig. 4c, d), respectively. As the concentration of fluorescent dyes increases, the emission peak of 2PACz@PVA in both SSPL and delayed PL spectra significantly diminishes (Supplementary Figs. 57–59), indicating the possibility of energy transfer from the singlet and triplet of 0.5 wt.% 2PACz@PVA to the doped fluorescence dyes. The optimized doping concentrations for Fluc@2PACz@PVA, Rh123@2PACz@PVA, and Rh6G@2PACz@PVA are 0.15, 0.25 and 0.15 wt.%, respectively, owing to their maximum delayed PL intensities. The SSPL and delayed PL spectra of Fluc@2PACz@PVA, Rh123@2PACz@PVA, and Rh6G@2PACz@PVA are almost identical to those of the corresponding Fluc, Rh123, and Rh6G doped PVA films, suggesting that the emerged peaks are attributed to the inherent emission of doped fluorescent dyes (Supplementary Fig. 60). The excitation-delayed PL mappings of 0.15 wt.% Fluc@2PACz@PVA, 0.25 wt.% Rh123@2PACz@PVA and 0.15 wt.% Rh6G@2PACz@PVA demonstrate nearly the same excitation range as the 2PACz@PVA (Supplementary Fig. 61), showing excitation wavelengths ranging from 220 to 350 nm. This means that these four doped films may have the same emission origin. Moreover, when directly exciting the fluorescent doped PVA films by 299 nm UV light, no observed afterglow emission can be captured, confirming the critical role of the energy donor of 2PACz@PVA film in triggering the multicolor afterglow emissions (Supplementary Fig. 62). Excitingly, this energy transfer process enables the afterglow emission to change from blue for 0.5 wt.% 2PACz@PVA to green (0.15 wt.% Fluc@2PACz@PVA), yellow (0.25 wt.% Rh123@2PACz@PVA), and red (0.15 wt.% Rh6G@2PACz@PVA) emissions as verified by the afterglow photographs (Supplementary Fig. 63), Commission International de l'Eclairage coordinates (Fig. 4e and Supplementary Fig. 64), and TRES spectra (Supplementary Fig. 65).

To further investigate the underlying mechanism of energy transfer, the lifetime analyses of 0.15 wt.% Fluc@2PACz@PVA, 0.25 wt.% Rh123@2PACz@PVA and 0.15 wt.% Rh6G@2PACz@PVA films were performed. The lifetimes at 370 nm have a significant decrease when the fluorescent guest is doped into 2PACz@PVA film at varied doping concentrations from 0.05 to 0.35 wt.% (Supplementary Fig. 66). Furthermore, the lifetimes of afterglow emission bands at 444 nm are decreased from 3.05 to 1.42 s for Fluc@2PACz@PVA films, from 3.05 to 0.80 s for Rh123@2PACz@PVA films, and from 3.05 to 1.15 s for Rh6G@2PACz@PVA films, respectively (Fig. 4f–h, Supplementary Figs. 67–69). Fluc@2PACz@PVA, Rh123@2PACz@PVA, and Rh6G@2PACz@PVA doped films exhibit no detectable long-lived afterglow when the fluorescent dyes are directly excited (Supplementary Fig. 70). These results indicate that non-radiative FRET process should be responsible for the multicolor afterglow emissions, enabling both FRET-dominated processes from the singlet and triplet excited states of the energy donor to the singlet excited state of the energy acceptor. Based on the amplitude lifetimes of fluorescence at 370 nm and the afterglow emission bands at 444 nm, the maximum FRET efficiencies of fluorescence can reach 29.8, 55.0, and 40.2%, and of afterglow can reach 59.2, 83.9, and 69.1% for Fluc@2PACz@PVA, Rh123@2PACz@PVA, and Rh6G@2PACz@PVA films, respectively (Supplementary Table 4).

Chiral multicolor afterglow emission exploration

To achieve COA emission, double-layer stacked polymeric films containing a top chiral polarizer of PLA layer and a bottom multicolor afterglow layer were constructed. These stacked films can be easily fabricated by spinning chiral PLA film onto multicolor afterglow films (Supplementary Fig. 71). Circularly polarized luminescence (CPL) spectra measurements are outlined in Supplementary Fig. 72a. As shown in Supplementary Figs. 73 and 74, using 0.5 wt.% 2PACz@PVA film as a model emitter, the concentrations of PLA solution were firstly optimized. Due to the largest dissymmetry factor (g_{lum}) of -3.0×10^{-2} (Fig. 5a–c), the optimized concentration of PLA is chosen as 100 mg mL^{-1}, showing a corresponding thickness of 6.5 μm (Supplementary Fig. 75). The stacked films show much improved CPL performance than that of films prepared via direct doping of 2PACz@PVA into the PLA matrix (Supplementary Fig. 76). Furthermore, compared with recently reported CPOA materials (Supplementary Table 5), the g_{lum} achieved in 2PACz@PVA@D/L-PLA ranks among the highest

https://doi.org/10.1038/s41467-026-69324-0

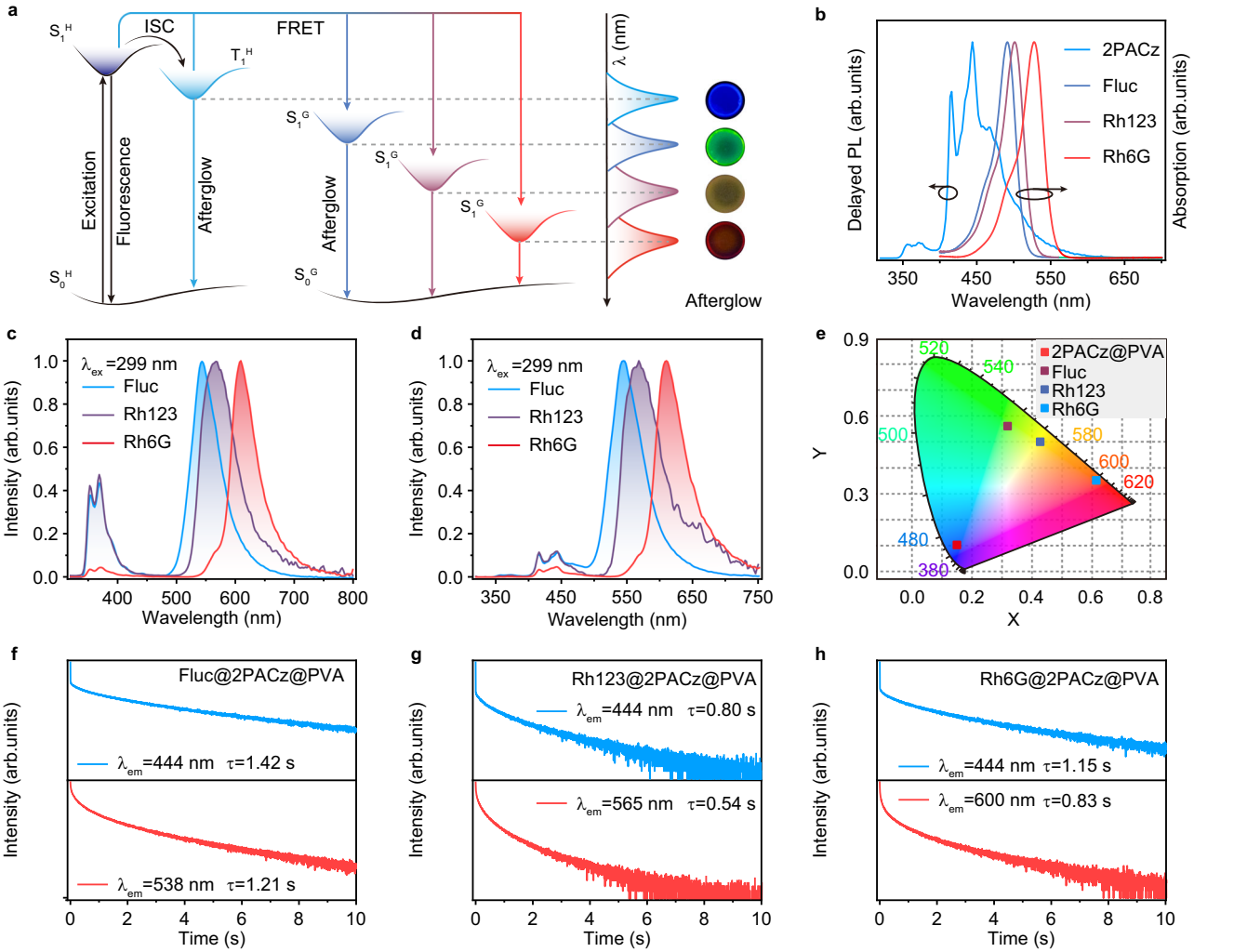

Fig. 4 | The photophysical properties investigation of colorful organic afterglow under ambient conditions. a Mechanism demonstration for multicolor emission based on Förster resonance energy transfer. **b** Delayed PL spectrum of 0.5 wt.% 2PACz@PVA film and absorption spectra of fluorescein sodium (Fluc), rhodamine 123 (Rh123), and rhodamine 6G (Rh6G) in aqueous solution (~10^{-5} mol L^{-1}). SSPL (**c**) and delayed PL (**d**) spectra of 0.15 wt.% Fluc, 0.25 wt.% Rh123 and 0.15 wt.% Rh6G doped 0.5 wt.% 2PACz@PVA films, respectively. **e** Commission Internationale de l'Eclairage 1931 coordinates of afterglow emission of 0.15 wt.% Fluc@2PACz@PVA, 0.25 wt.% Rh123@2PACz@PVA and 0.15 wt.% Rh6G@2PACz@PVA films. **f** Afterglow decay profiles of emission bands at 444 nm (top panel) and 538 nm (bottom panel) of 0.15 wt.% Fluc@2PACz@PVA film. **g** Afterglow decay profiles of emission bands at 444 nm (top panel) and 565 nm (bottom panel) of 0.25 wt.% Rh123@2PACz@PVA film. **h** Afterglow decay profiles of emission bands at 444 nm (top panel) and 600 nm (bottom panel) of 0.15 wt.% Rh6G@2PACz@PVA film.

values reported to date. Interestingly, due to the polarized feature of PLA film, reversed CPL signals could be achieved when the excitation UV light is placed in front of and behind the 2PACz@PVA@PLA film (Supplementary Figs. 72, 77 and 78)[56–58]. Therefore, distinct green, yellow, and red COA with emission peak at 538, 565, and 600 nm and g_{lum} of 5.2×10^{-3}, 5.1×10^{-3}, and 2.2×10^{-3} are achieved by spinning D/L-PLA films onto the top of 0.15 wt.% Fluc, 0.25 wt.% Rh123, and 0.15 wt.% Rh6G doped 2PACz@PVA films, respectively (Fig. 5d–f). Compared to the pure luminescent films, the stacked films coated with PLA polarizer show slightly decreased PLQYs (Supplementary Table 6). Exposure to high humidity substantially (Supplementary Fig. 79) reduces afterglow emissions. After 4 h of 365 nm irradiation, the afterglow retains ~77% intensity (Supplementary Fig. 80). Due to suppressed exciton thermal quenching (Supplementary Fig. 81), decreased temperature significantly enhances the CPL intensity. With the temperature increased, the CPL intensity of 2PACz@PVA@D/L-PLA is slightly decreased, which is much higher than that of 4PACz@PVA@D/L-PLA and 2CACz@PVA@D/L-PLA (Supplementary Fig. 82).

Potential applications of chiral multicolor afterglow polymers

Due to the efficient afterglow and chirality of the stacked polymers, luminescent coating film, anti-counterfeiting encryption, and writable afterglow ink were achieved. As shown in Fig. 6a, an aqueous solution of 2PACz@PVA is directly dropped onto the surface of coin (Supplementary Fig. 83), and after drying, afterglow films with visible surface details of the coin as well as flexibility and transparency are obtained (Supplementary Fig. 84).

Furthermore, a quick response (QR) code prepared through screen printing (Supplementary Fig. 85) is invisible due to background fluorescence interference. However, after removing the UV light, the QR code is clearly observed, and "COO" information can be readable by a mobile phone (Fig. 6b). Due to the appropriate water-solubility and long lifetime of 2PACz@PVA, 0.15 wt.% Fluc@2PACz@PVA, 0.25 wt.% Rh123@2PACz@PVA and 0.15 wt.% Rh6G@2PACz@PVA, the aqueous solutions were used as afterglow inks (Fig. 6c). Multicolor afterglow characters can be easily written and captured (Fig. 6d). By using 2PACz@PVA, Fluc@2PACz@PVA, Rh123@2PACz@PVA, and

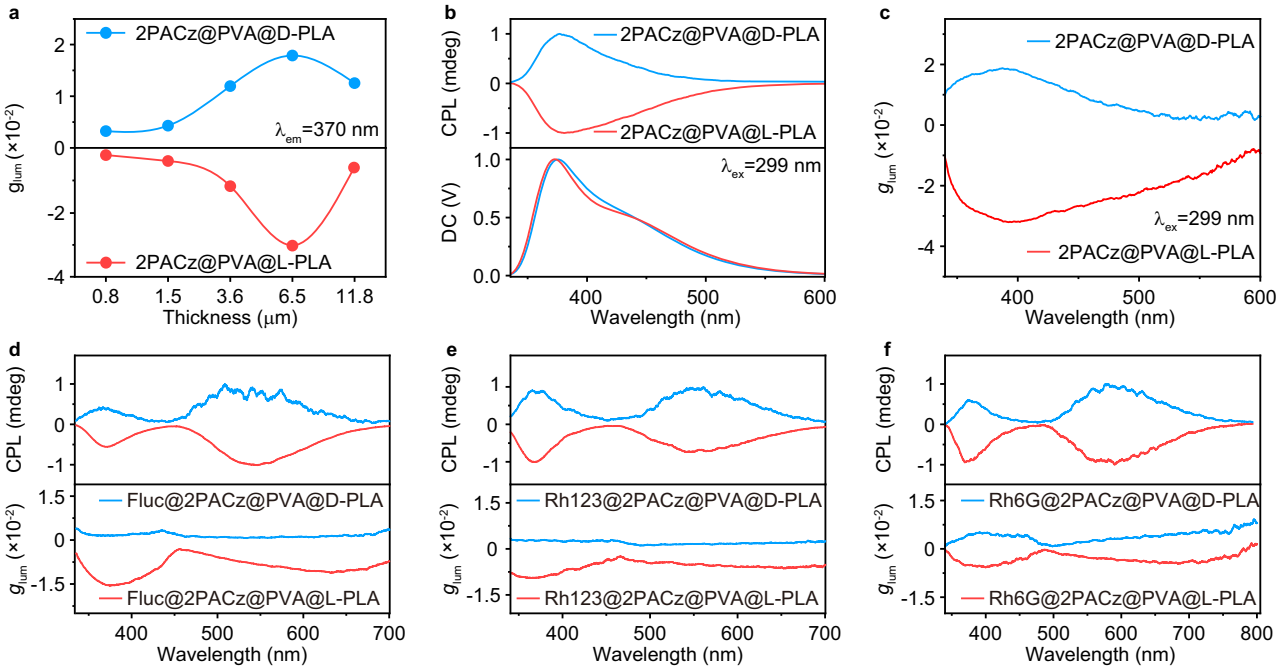

Fig. 5 | Exploration of multicolor COA in a double-layer stacked polymeric film. **a** The dissymmetry factor (g_{lum}) of 2PACz@PVA@D/L-PLA films with different thickness of chiral PLA film. Circularly polarized luminescence (CPL) spectra (**b**) and g_{lum} (**c**) of 2PACz@PVA@D/L-PLA films. CPL spectra and g_{lum} of 0.15 wt.% Fluc@2PACz@PVA@D/L-PLA (**d**), 0.25 wt.% Rh123@2PACz@PVA@D/L-PLA (**e**), and 0.15 wt.% Rh6G@2PACz@PVA@D/L-PLA films (**f**). Noted: The stacked polymeric films feature a strategically designed bilayer multicolor afterglow and chiral PLA film, where incident photons primarily interact with the multicolor afterglow film prior to penetrating chiral PLA film. The thickness of the chiral PLA layer is 6.5 μm and the doping concentration of 2PACz in PVA film is 0.5 wt.%.

Rh6G@2PACz@PVA as emitters, a 3 × 4 encoding luminescent matrix was prepared. In principle, the color of blue, green, yellow, and red were defined as Morse code symbols of "●," "●●," "▬," and "●▬," respectively (Fig. 6e and Supplementary Text 1). Upon UV light irradiation, a luminescent matrix exhibits the information of "4VLP". When the UV lamp is turned off, an afterglow encoded matrix with information of "4ALP" is captured. Moreover, due to the chiral polarizer of PLA, the chiral afterglow encoded information of "HELP" is observable, thereby achieving multiple encryptions.

Discussion

In summary, we have successfully developed a multicolor COA system in a stacked polymer through the integration of phosphorus-mediated hydrogen bond, phosphorescence energy transfer, and chiral polarization. By manipulating the electronegativity and directionality of hydrogen bonds through phosphate groups, more linear and stronger hydrogen bonds with PVA are enabled, resulting in a polymeric film with a blue afterglow emission lifetime and PLQY of 3.05 s and 33.3%. With the aid of the energy transfer strategy and chiral polarizer, multicolor chiral luminescent polymers have been achieved, endowing blue, green, yellow, and red COA emissions with luminescent peaks at 444, 538, 565, and 600 nm and g_{lum} of 3.0×10^{-2}, 5.2×10^{-3}, 5.1×10^{-3}, and 2.2×10^{-3}. The high water-solubility, transparency, and flexibility of the polymeric films make them ideal candidates for a range of applications, including high-resolution afterglow casting film, afterglow ink, and anti-counterfeiting encryption. This work not only offers a deep insight into the regulation of hydrogen bond interaction for modulating the afterglow properties but also provides an ideal platform for the development of advanced afterglow applications.

Methods

Materials

Chemical reagents, unless otherwise specified, were purchased from Energy Chemical, Acros, or Alfa Aesar, and used without further purification. The polyvinyl alcohol (PVA) was purchased from Sigma-Aldrich (Mw=85000-124000).

Preparation procedure of films

General fabrication procedure for fabricating 0.5 wt.% 2PACz@PVA (polyvinyl alcohol) film: Firstly, 2.5 mg of 2PACz was dissolved into 1 mL of ethanol. 0.5 g of PVA polymers was dissolved into 5 mL of distilled water and stirred at 90°C for 0.5 h to obtain 100 mg mL^{-1} of PVA solution. 1 mL 2PACz ethanol solution was added into 5 mL of PVA aqueous solution and mixed at 90°C for 0.5 h. Then, the mixture was dropped on a 2 × 2 cm^2 quartz sheet and dried in an oven at 70°C for 12 h to fabricate transparent polymer films for subsequent photophysical and morphological characterizations. The same procedure is used to obtain the 4PACz@PVA and 2CACz@PVA films with different doping concentrations.

Instrumentation

^1H and ^{13}C-nuclear magnetic resonance (NMR) spectra were recorded on a Bruker Ultra Shield Plus 400 MHz instrument with dimethyl sulfoxide (DMSO)-d_6 as the solvent and tetramethyl silane as the internal standard. ^{31}P-NMR was recorded on a Bruker Ultra Shield Plus 400 MHz instrument with DMSO-d_6 as the solvent and phosphoric acid as the internal standard. Ultraviolet-visible absorption spectra were recorded on a Jasco V-750 spectrophotometer. Steady-state photoluminescence spectra were recorded on an Edinburgh FLS 1000 fluorescence spectrophotometer. The delayed PL spectra in dilute tetrahydrofuran were obtained using an Edinburgh FLS 1000 fluorescence spectrophotometer at 77 K in a dewar vessel with a 10 ms delay time using a microsecond (μs) flash lamp. The microsecond flash lamp produces short, typically a few μs, and high irradiance optical pulses for decay measurements in the range from microseconds to seconds. The delayed PL spectra and ultralong lifetimes were also measured using an Edinburgh FLS 1000 fluorescence spectrophotometer. For fluorescence lifetime measurements, a picosecond pulsed light-

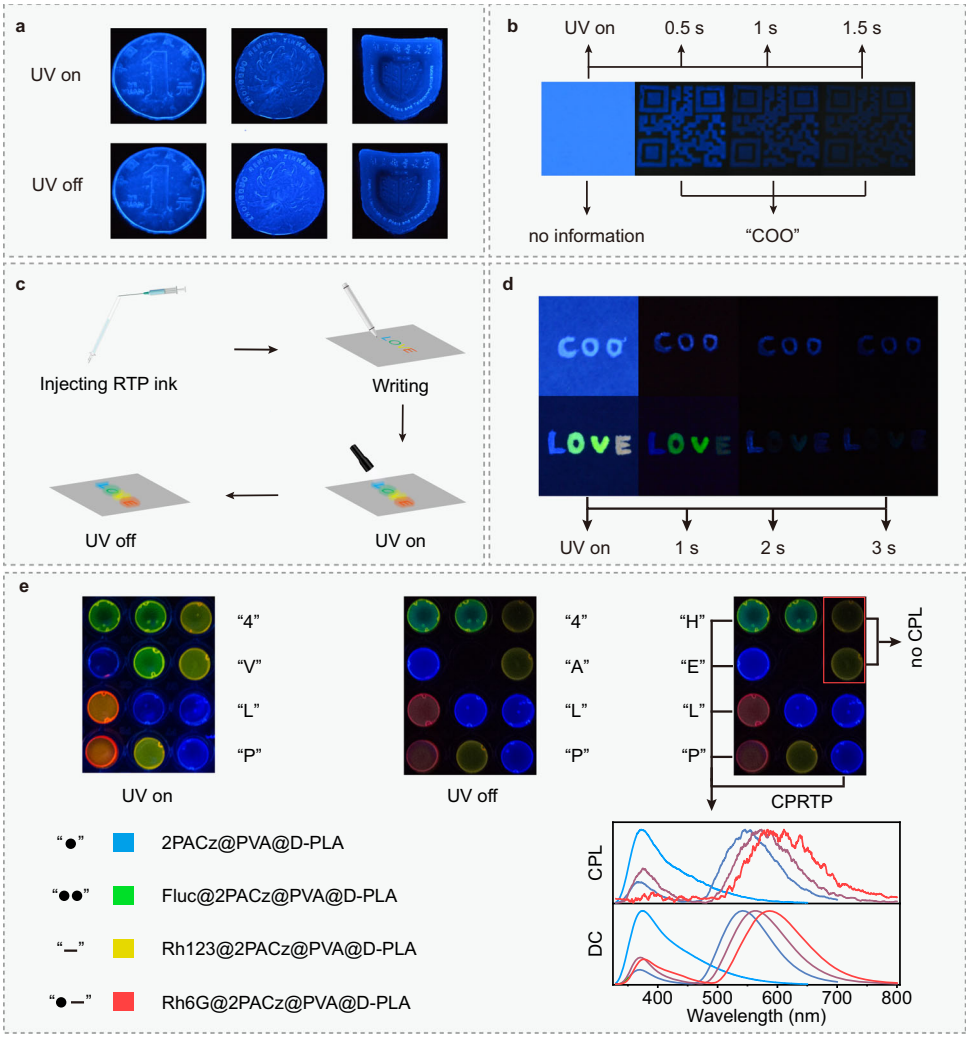

Fig. 6 | Potential applications of multicolor COA polymers. a Afterglow photographs of luminescent coating film. **b** Photographs of afterglow quick response code. Schematic diagram (**c**) and corresponding photographs (**d**) of multicolor afterglow inks. **e** Multiple information Morse code encrypted by colorcode.

emitting diode (EPLED-290, wavelength: 300 nm; pulse width: 833.7 ps) was used. Excitation-PL mapping was measured using Hitachi F-4700 under ambient conditions. Powder X-ray diffractometry (XRD) patterns were measured using a Bruker D8 Advance diffractometer (Cu Kα: λ = 1.5418 Å) under ambient conditions. The Fourier transform infrared (FTIR) spectra were obtained using Nicolet IN10 micro-spectroscopy (Thermo Fisher Scientific). The thickness of the chiral films was measured using a DektakXT step meter, with a stylus scan range of 65 μm, a scanning length of 400 μm, a scan duration of 10 s, and a scan resolution of 0.13 μm. The intrinsic circularly polarized luminescence (CPL) spectra were investigated using a JASCO CPL-300 spectrometer. The scan speed was set as 500 nm min^{-1} with 0.1 nm resolution and a response time of 1.0 s.

Theoretical calculation

The geometric structure of the ground state was optimized using density functional theory. The frequency was then calculated and analyzed at the same level to confirm that the optimized geometric structure is a stable configuration. The excited state was calculated using time-dependent density functional theory using a universal B3LYP hybrid functional and 6-31G (d) basis set, and combining with DFT-D3 (BJ) dispersion correction due to the involvement of weak interactions. All theoretical calculations were performed under the Gaussian09 D.01 package, and the frontier molecular orbitals were plotted using GaussView 6.0 software. The static potential and weak interaction energy were analyzed using the Multiwfn 3.8 package, and images of static potential and independent gradient model based on Hirshfeld partition were obtained through Visual Molecular Dynamics software. The spin-orbit coupling matrix elements between singlet and triplet states were calculated using ORCA software.

Data availability

The main data generated in this study are provided in the Source data file. The data that support the plots of this study are available from the corresponding author on request. Source data are provided with this paper.

References

1. Kabe, R. & Adachi, C. Organic long persistent luminescence. *Nature* **550**, 384–387 (2017).
2. Zhang, L., Wang, H.-X., Li, S. & Liu, M. Supramolecular chiroptical switches. *Chem. Soc. Rev.* **49**, 9095–9120 (2020).
3. Nie, F., Wang, K.-Z. & Yan, D. Supramolecular glasses with color-tunable circularly polarized afterglow through evaporation-induced self-assembly of chiral metal-organic complexes. *Nat. Commun.* **14**, 1654 (2023).

4. Li, H. et al. Purely organic room temperature phosphorescent materials toward organic light-emitting diodes. *FlexMat* **1**, 173–192 (2024).
5. Zhou, Q. et al. [5] Helicene based π-conjugated macrocycles with persistent figure-eight and möbius shapes: efficient synthesis, chiral resolution and bright circularly polarized luminescence. *Angew. Chem. Int. Ed.* **137**, e202417749 (2025).
6. Ji, M.-J., Zhao, W.-L., Li, M. & Chen, C.-F. Circularly polarized luminescence with high dissymmetry factors for achiral organic molecules in solutions. *Nat. Commun.* **16**, 2940 (2025).
7. Li, H. et al. Enabling multicolor circularly polarized organic long persistent luminescence through chiral exciplex. *Adv. Mater.* **37**, 2500841 (2025).
8. Li, H. et al. Single-component color-tunable circularly polarized organic afterglow through chiral clusterization. *Nat. Commun.* **13**, 429 (2022).
9. Liu, H. et al. Multicolor-tunable room-temperature afterglow and circularly polarized luminescence in chirality-induced coordination assemblies. *Chem. Sci.* **13**, 13922–13929 (2022).
10. Wang, T. et al. Long-lived charge separation induced organic long-persistent luminescence with circularly polarized characteristic. *Adv. Opt. Mater.* **11**, 2202613 (2023).
11. Zhang, Y. et al. Enhanced photoactivated circularly polarized afterglow with high dissymmetry factor and tunable emission. *Adv. Funct. Mater.* **35**, 2424404 (2025).
12. Chen, B., Huang, W. & Zhang, G. Observation of chiral-selective room-temperature phosphorescence enhancement via chirality-dependent energy transfer. *Nat. Commun.* **14**, 1514 (2023).
13. Chen, X. et al. Rapid room-temperature phosphorescence chiral recognition of natural amino acids. *Nat. Commun.* **15**, 3314 (2024).
14. Gao, Z. et al. Stimulating chiral selective expression of room temperature phosphorescence for chirality recognition. *Adv. Sci.* **11**, 2410671 (2024).
15. Zhang, M. et al. Processable circularly polarized luminescence material enables flexible stereoscopic 3D imaging. *Sci. Adv.* **9**, eadi9944 (2023).
16. Zheng, M. Y., Jin, Z. B., Ma, Z. Z., Gu, Z. G. & Zhang, J. Photo-curable 3D printing of circularly polarized afterglow metal-organic framework monoliths. *Adv. Mater.* **36**, 2313749 (2024).
17. Bolton, O., Lee, K., Kim, H.-J., Lin, K. Y. & Kim, J. Activating efficient phosphorescence from purely organic materials by crystal design. *Nat. Chem.* **3**, 205–210 (2011).
18. Xia, J. et al. Near-infrared circularly polarized organic room temperature phosphorescence based on a chiral host–guest doping strategy. *J. Phys. Chem. C* **12**, 9578–9585 (2024).
19. Zhang, K. et al. Multi-stimuli-responsive circularly polarized luminescence with handedness inversion and near-infrared phosphorescence in chiral metal-organic framework platform for white light emission and information encryption. *Adv. Sci.* **12**, 2502784 (2025).
20. Zhang, C. et al. Organic room temperature phosphorescence co-crystal with reversible acid/base stimulus response. *Smart Mol.* **3**, e20240054 (2025).
21. Zhang, C. et al. Self-confining isolated chiral chromophore for circularly polarized organic afterglow from amorphous polymer systems. *Chem. Eng. J.* **485**, 149886 (2024).
22. Xiao, Y. et al. Construction of multi-decay pathways and realizing polymer-regulated organic smart luminescent materials. *FlexMat* **1**, 193–202 (2024).
23. You, J. et al. Responsive circularly polarized ultralong room temperature phosphorescence materials with easy-to-scale and chiral-sensing performance. *Nat. Commun.* **15**, 7149 (2024).
24. Song, Z. P. et al. Mechanically-tunable and full-color circularly polarized long-lived phosphorescence in chiral superstructure elastomers. *Adv. Mater.* **37**, 2419640 (2025).
25. Yang, Y. et al. Photo-response with radical afterglow by regulation of spin populations and hole-electron distributions. *Angew. Chem. Int. Ed.* **135**, e202218994 (2023).
26. Guo, G. et al. A dynamic H-bonding network enables stimuli-responsive color-tunable chiral afterglow polymer for 4D encryption. *Adv. Mater.* **36**, 2412100 (2024).
27. Lin, F. et al. Stepwise energy transfer: near-infrared persistent luminescence from doped polymeric systems. *Adv. Mater.* **34**, 2108333 (2022).
28. Li, D. et al. Completely aqueous processable stimulus responsive organic room temperature phosphorescence materials with tunable afterglow color. *Nat. Commun.* **13**, 347 (2022).
29. Zhang, Y. et al. Rational molecular and doping strategies to obtain organic polymers with ultralong RTP. *Chem. Sci.* **14**, 5177–5181 (2023).
30. Lu, Y., Chen, X., Suh, Y. D. & Liu, X. Combinatorial discovery of small molecule-doped afterglow polymer composites for anti-counterfeiting. *FlexMat* **2**, 107–114 (2024).
31. Zhang, Y. et al. Cross-linked polyphosphazene nanospheres boosting long-lived organic room-temperature phosphorescence. *J. Am. Chem. Soc.* **144**, 6107–6117 (2022).
32. Li, T. et al. Crosslink-enhanced strategy to achieve multicolor long-lived room temperature phosphorescent films with excellent photostability. *Chin. Chem. Lett.* **33**, 4238–4242 (2022).
33. Su, Y. et al. Excitation-dependent long-life luminescent polymeric systems under ambient conditions. *Angew. Chem. Int. Ed.* **132**, 10053–10057 (2020).
34. Chen, D. et al. Achieving high-temperature resistant afterglow by modulating dual-mode emission of organic emitters through defects engineering. *Small* **21**, 2409689 (2025).
35. Tang, S. et al. Cycloolefin copolymers with a multiply rigid structure for protecting triplet exciton from thermo-and moisture-quenching. *Adv. Mater.* **37**, 2416397 (2025).
36. Platts, J. A., Howard, S. T. & Bracke, B. R. F. Directionality of hydrogen bonds to sulfur and oxygen. *J. Am. Chem. Soc.* **118**, 2726–2733 (1996).
37. Bonn, M. & Hunger, J. Between a hydrogen and a covalent bond. *Science* **371**, 123–124 (2021).
38. Morris, D. T. J. et al. Dynamic and persistent cyclochirality in hydrogen-bonded derivatives of medium-ring triamines. *J. Am. Chem. Soc.* **145**, 19030–19041 (2023).
39. Grayson, M. N., Yang, Z. & Houk, K. N. Chronology of CH···O hydrogen bonding from molecular dynamics studies of the phosphoric acid-catalyzed allylboration of benzaldehyde. *J. Am. Chem. Soc.* **139**, 7717–7720 (2017).
40. Choudhury, R. R. & Chitra, R. Investigation of nuclear quantum effect on the hydrogen bonds of ammonium dihydrogen phosphate using single-crystal neutron diffraction and theoretical modelling. *Pramana J. Phys.* **91**, 53 (2018).
41. Kawashima, Y., Sawada, K., Nakajima, T. & Tachikawa, M. A path integral molecular dynamics study on intermolecular hydrogen bond of acetic acid-arsenic acid anion and acetic acid-phosphoric acid anion clusters. *J. Comput. Chem.* **40**, 172–180 (2019).
42. Stevensson, B. & Edén, M. Metadynamics simulations of the pH-dependent adsorption of phosphoserine and citrate on disordered apatite surfaces: What interactions govern the molecular binding?. *J. Phys. Chem. C* **125**, 11987–12003 (2021).
43. Bunn, C. W. Crystal structure of polyvinyl alcohol. *Nature* **161**, 929–930 (1948).
44. Wang, Z.-L. et al. Responsive hybrid poly(vinyl alcohol) hydrogel membranes with embedded microgels as valves. *Chin. J. Polym. Sci.* **41**, 1646–1655 (2023).
45. Takeno, H., Inoguchi, H. & Hsieh, W.-C. Mechanical and structural properties of cellulose nanofiber/poly (vinyl alcohol) hydrogels

cross-linked by a freezing/thawing method and borax. *Cellulose* **27**, 4373–4387 (2020).
46. Li, D., Yang, J., Fang, M., Tang, B. Z. & Li, Z. Stimulus-responsive room temperature phosphorescence materials with full-color tunability from pure organic amorphous polymers. *Sci. Adv.* **8**, eabl8392 (2022).
47. Zhao, X. et al. Designable polypyrrole pattern in hydrogel achieved by photo-controllable concentration of Fe^{3+} initiator. *Smart Mol.* **2**, e20240015 (2024).
48. Li, X. et al. Bright and ultralong organic phosphorescence via sulfonic acid functionalization for high-contrast real-time light-writing display. *J. Am. Chem. Soc.* **147**, 14198–14210 (2025).
49. Kolesov, B. A. Hydrogen bonds: Raman spectroscopic study. *Int. J. Mol. Sci.* **22**, 5380 (2021).
50. Latimer, W. M. & Rodebush, W. H. Polarity and ionization from the standpoint of the Lewis theory of valence. *J. Am. Chem. Soc.* **42**, 1419–1433 (1920).
51. Riley, K. E. Critical comparison of RX···Y and RH···Y directionality in halogen and hydrogen bonds using modern computational chemistry methods. *Chem. Phys. Lett.* **744**, 137221 (2020).
52. Akkerman, H. B. et al. Effects of odd-even side chain length of alkyl-substituted diphenylbithiophenes on first monolayer thin film packing structure. *J. Am. Chem. Soc.* **135**, 11006–11014 (2013).
53. Cho, I. et al. Exploiting intermolecular interactions between alkyl-functionalized redox-active molecule pairs to enhance interfacial electron transfer. *J. Am. Chem. Soc.* **140**, 13935–13944 (2018).
54. Peng, H. et al. On-demand modulating afterglow color of water-soluble polymers through phosphorescence FRET for multicolor security printing. *Sci. Adv.* **8**, eabk2925 (2022).
55. Zeng, M. et al. Enabling robust blue circularly polarized organic afterglow through self-confining isolated chiral chromophore. *Nat. Commun.* **15**, 3053 (2024).
56. Gao, X., Wang, J., Yang, K., Zhao, B. & Deng, J. Regulating the helical chirality of racemic polyacetylene by chiral polylactide for realizing full-color and white circularly polarized luminescence. *Chem. Mater.* **34**, 6116–6128 (2022).
57. Gao, X., Zhao, B. & Deng, J. Chirality transfer from polylactide to achiral fluorophore in hierarchical crystallization for realizing handedness-tunable and nonreciprocal circularly polarized luminescence. *Macromolecules* **55**, 10618–10627 (2022).
58. Ma, S. et al. Intense circularly polarized fluorescence and room-temperature phosphorescence in carbon dots/chiral helical polymer composite films. *ACS Nano* **17**, 6912–6921 (2023).

Acknowledgements

This study was supported in part by the National Natural Science Foundation of China (22322106 awarded to Y.T., 22075149 awarded to Y.T., 62075102 awarded to Huanhuan Li, 22105104 awarded to G.X., 22305126 awarded to Hui Li, and 62288102 awarded to W.H.), Basic Research Program of Jiangsu (BK20243057 awarded to W.H.), U35 Strong Foundation Program of Nanjing (awarded to Y.T.), the Hua Li Talents Program of Nanjing University of Posts and Telecommunications (awarded to Y.T.), and Postgraduate Research & Innovation Program of Jiangsu Province (KYCX23-0979 awarded to Z.G., KYCX24-1137 awarded to X.Y., KYCX24-1146 awarded to S.Z. and KYCX25-1195 awarded to H.C.).

Author contributions

Z.G. and Huanhuan Li synthesized and characterized the materials, processed and plotted the experimental data. S.H., X.L., X.Y., H.C., S.Z., and Q.J. carried on the partial supplemented data and revised the manuscript. P.Z. performed theoretical calculations. Huanhuan Li, Hui Li, R.C., G.X., Y.M., and T.W. provided helpful discussions on the synthesis and testing. Y.T. and W.H. supervised this work, wrote the manuscript, and were responsible for funding acquisitions.

Competing interests

The authors declare no competing interests.

Additional information

Supplementary information The online version contains supplementary material available at https://doi.org/10.1038/s41467-026-69324-0.

Correspondence and requests for materials should be addressed to Huanhuan Li, Wei Huang or Ye Tao.

Peer review information *Nature Communications* thanks Krzysztof Durka and Shanfeng Xue for their contribution to the peer review of this work. A peer review file is available.